Received: 3 September 2023 | Revised: 13 January 2024 | Accepted: 28 February 2024

IET Microwaves, Antennas & Propagation

DOI: 10.1049/mia2.12471

ORIGINAL RESEARCH

Mechanical azimuthal beam-steering Fabry–Perot resonator antenna with large deflection angle

Yufeng Liu[1] | Lele Zhu[1] | Wenmei Zhang[1] | Wensong Wang[2]

[1]School of Physics and Electronic Engineering, Shanxi University, Taiyuan, Shanxi, China

[2]School of Electrical and Electronic Engineering Nanyang Technological University, Jurong West, Singapore

Correspondence

Yufeng Liu.
Email: liuyufeng@sxu.edu.cn

Funding information

National Natural Science Foundation of China, Grant/Award Number: 62071282

Abstract

Continuous beam steering approach with minimal power consumption is highly desirable in modern antenna designs. A simple mechanical method for achieving beam steering in the Fabry–Perot resonator antenna (FPRA) is presented. It involves rotating the upper phase gradient metasurface (PGM) mechanically to change the aperture phase distribution, so the beam is continuously steered in the azimuthal plane while maintaining a large elevation angle. The proposed PGM unit cell comprises a hexagonal ring and patch printed on both sides of the substrate, along with a honeycomb lattice. A prototype antenna operating at 5.65 GHz is fabricated and measured to validate the feasibility. Measurement results show that the FPRA achieves a gain of 14.9 dBi, and can continuously steer its beam in the azimuthal plane with an elevation angle of around $\theta = 50°$. Measured radiation patterns in eight azimuthal directions ($\varphi = 0°, 45°, 90°, 135°, 180°, 225°, 270°$, and $315°$) are consistent with the simulated results. Compared with other electrical tuning methods, our design has a compact size and requires lower power for the PGM rotation.

KEYWORDS

beam steering, Fabry-Perot resonators

1 | INTRODUCTION

With the rapid development of modern communication technology, reconfigurable antennas, and metasurfaces have drawn a great deal of attention [1–3]. The concept of a reconfigurable antenna was first proposed by Schaubert et al. in 1983 [4]. The radiation pattern reconfigurable antenna has been extensively studied due to its potential to enhance the quality and security of wireless communication systems while mitigating noisy environments [5–8].

The Fabry–Perot resonant antenna (FPRA) is a widely used high-gain antenna design that is typically constructed by placing a partially reflective surface (PRS) above a primary radiator and a ground plane to create a resonant cavity. FPRAs provide the advantages of reduced size, simplified structure, and lower cost [9–11]. In addition to their high gain characteristics, FPRAs can also achieve beam steering capabilities, and numerous significant studies on this subject have been documented [12–17].

Currently, electrical and mechanical techniques are the most commonly used methods for beam steering. Beam reconfigurable FPRA systems based on electrical control can be achieved by incorporating semiconductor devices like PIN diodes and varactor diodes. For example, in refs. [12, 13], Ji et al. realised beam tilt by introducing PIN diodes into PRS. In refs. [14, 15], Guzmán-Quirós et al. developed a tunable high impedance surface equipped with varactor diodes, enabling continuous electronic beam scanning. The mechanical technique serves as an alternative approach to beam steering. For example, in ref. [16], Yang et al. designed a simple method to control radiation patterns by injecting liquid metal into specific zones of the PRS. In ref. [17], a bianisotropic metasurface (BMS) is employed as the PRS, and slight rotation of the BMS results in beam-steering capabilities. In ref. [18], an anisotropic Huygens metasurface is positioned in front of a horn antenna, allowing the alteration of the main beam through metasurface rotation.

Electrical beam steering offers the advantage of faster real-time tracking and programmability, but it involves multiple

phase-shifter components and a relatively complex bias network. Even when the beam direction is fixed, the antenna still requires an electrical power supply. However, in recently published study [19–21], continuous beam steering can be achieved by mechanically rotating a double-layer frequency selective surface. In contrast, the mechanical technique exhibits a slower scanning speed. But it significantly reduces complexity and requires less energy to sustain the mechanical motion. Thus, the mechanical method is a promising technology for beam steering.

This study utilises a novel phase gradient metasurface (PGM) to achieve beam steering in the FPRA. The PGM, proposed by Yu et al. [22], has been extensively investigated for beam manipulations [23–27]. The proposed PGM employs complementary hexagonal unit cells arranged in honeycomb lattices, providing an additional degree of freedom compared to other unit cell shapes. Moreover, the hexagonal topology allows for a smaller aperture size due to the reduced effective inter-element spacing compared to the conventional square lattice [28]. Continuous 360° beam steering in the azimuthal plane is achieved by rotating the PGM around the centre with respect to the feed source. The rotation scheme can be potentially implemented using a step motor, which can be switched off when the beam is fixed, resulting in lower power consumption for the proposed FPRA. To validate the concept, a prototype antenna operating at 5.65 GHz is designed, fabricated, and measured, demonstrating continuous beam steering capabilities.

2 | PROPOSED FPRA AND DESIGN PROCEDURE

The proposed FPRA consists of a driven circular patch antenna and a tunable PGM as illustrated in Figure 1. The operational principles and the design methodology of the antenna are discussed below.

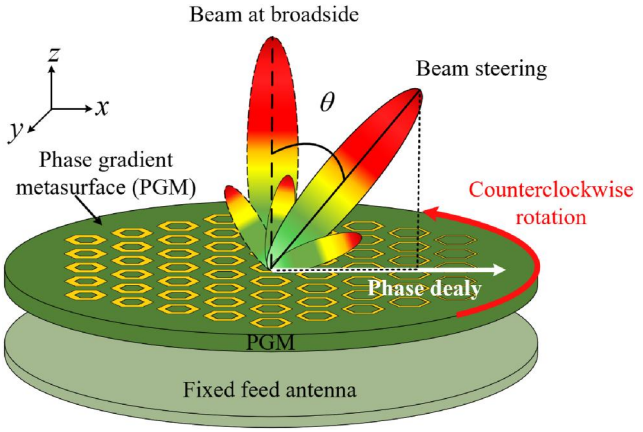

FIGURE 1 Perspective view of the proposed mechanical rotation PGM. PGM, phase gradient metasurface.

2.1 | Design method and principle

To achieve beam steering, a novel mechanical approach is presented for the rotation of the upper PGM. The PGM is designed with a specific phase delay in the x-axis direction and a uniform phase distribution in the orthogonal direction, resulting in a θ deflection in the elevation. Subsequent rotation of the PGM around the central axis of the aperture enables continuous steering of the initially fixed main beam in the azimuth plane.

In the design of PGM, it is essential for the incident and refracted waves to adhere to the generalised Snell's law [22]. Assuming a constant rate of phase change and an incident angle of 0°, the relationship between the phase gradient and the beam tilt angle can be expressed as follows:

$$\frac{d\phi}{dx} = \frac{2\pi}{\lambda_0}\sin\theta \tag{1}$$

where θ is the beam tilt angle, λ_0 is the operating wavelength, and $d\phi/dx$ represents the phase gradient. Taking a beam angle of $\theta = 50^{\circ}$ as an example, the corresponding phase gradient can be calculated as $d\phi/dx = 91.1$ rad/m.

The schematic view of the beam tilt FPRA is described in Figure 2. The radiator located above the floor radiates the electromagnetic wave (EW) at an angle of α. The radiation direction is $f(\alpha)$ and the magnitude is E_0. The PRS is located at a distance of H above the feed, and the EW radiated from the feed is partly reflected in the cavity, while the other part is constantly transmitted out of the PRS. Thus, the electric field amplitude of the far field of FPRA is the sum of all transmitted waves, which can be expressed as follows [29]:

$$E = \sum_{i=-\infty}^{+\infty} f(\alpha)E_i \tag{2}$$

$$E_i = E_0 T_i e^{j\psi_{Ti}} \prod_{n=1}^{i-1} R_n e^{j\varphi_n} \tag{3}$$

where $T_i e^{j\psi_{Ti}}$ represents the transmitted wave passing through PRS, T_i is the transmission coefficient of unit cell i, and ψ_{Ti} corresponds to the transmission phase. $\prod_{n=1}^{i-1} R_n e^{j\varphi_n}$ represents the reflected wave in the cavity, R_n is the reflection coefficient of the nth unit cell, φ_n means the phase shift caused by PRS reflection, the ground plane, and the path travelled by the EW, which can be calculated as follows [30]:

$$\varphi_i = \begin{cases} \dfrac{2\pi}{\lambda_0}\dfrac{H}{\cos\alpha}, & -1 \le i \le 1 \\ \dfrac{(2i-1)2\pi}{\lambda_0}\dfrac{H}{\cos\alpha} + (i-1)\pi + \sum_{k=0}^{i-1}\psi_{Rk}, & i \ge 2 \\ \dfrac{(-2i-1)2\pi}{\lambda_0}\dfrac{H}{\cos\alpha} + (-i-1)\pi + \sum_{k=0}^{i+1}\psi_{Rk} & i \le -2 \end{cases} \tag{4}$$

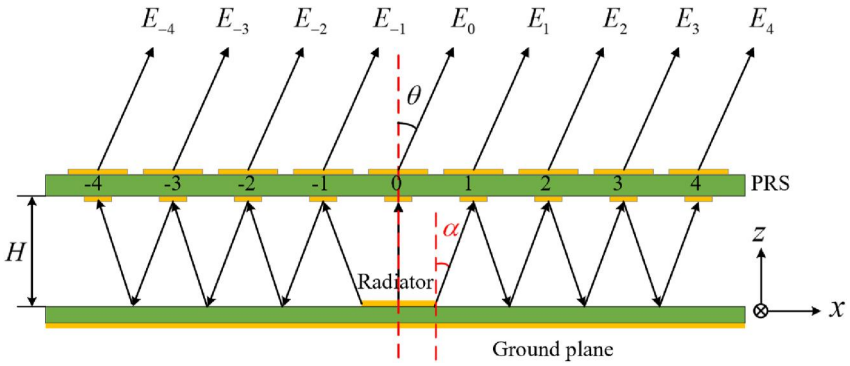

FIGURE 2 Schematic view of the beam tilt Fabry–Perot resonator antenna.

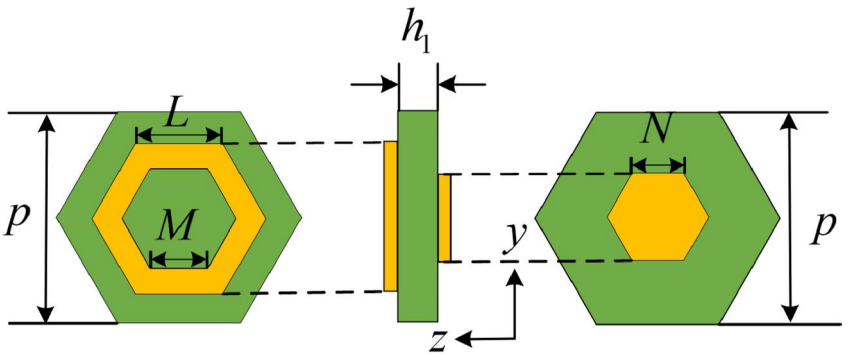

FIGURE 3 Geometry of the proposed phase gradient metasurface unit cell.

where $(2\pi/\lambda_0) = \beta$ is the phase shift constant, and ψ_{Rk} corresponds to the reflection phase of the kth unit cell. α can be calculated by $\alpha = \tan^{-1}(p/2H)$, and p corresponds to the unit cell period.

The beam deflection angle θ of the FPRA is determined by the phase difference $\Delta\varphi$ of the PRS unit cell, which includes the reflection phase and transmission phase of the unit cell and the phase difference caused by the wave path of EW radiated from the feed to the unit cell. In this paper, the phase of the unit cell is adjusted by changing the size of the unit cell, and the phase caused by the wave path can be calculated by using Equation (4).

2.2 | PGM unit cell design

The geometry of the proposed PGM unit cell is shown in Figure 3. Complementary hexagonal unit cell is designed on an FR4 substrate ($\varepsilon_r = 4.4$) with a thickness of $h_1 = 2.2$ mm. The advantage of the proposed unit cell arrangement can be inferred in Figure 4. Unlike circular, square, and decagon structures, the regular hexagonal unit cell can be arranged in a honeycomb structure, closely and periodically, along the D_1, D_2, and D_3 directions. When the unit cell period p is fixed, the dielectric substrate of the same aperture size can accommodate more regular hexagonal unit cells. As a result, the honeycomb lattice allows for a denser distribution of PGM unit cells, leading to a significant reduction in aperture size.

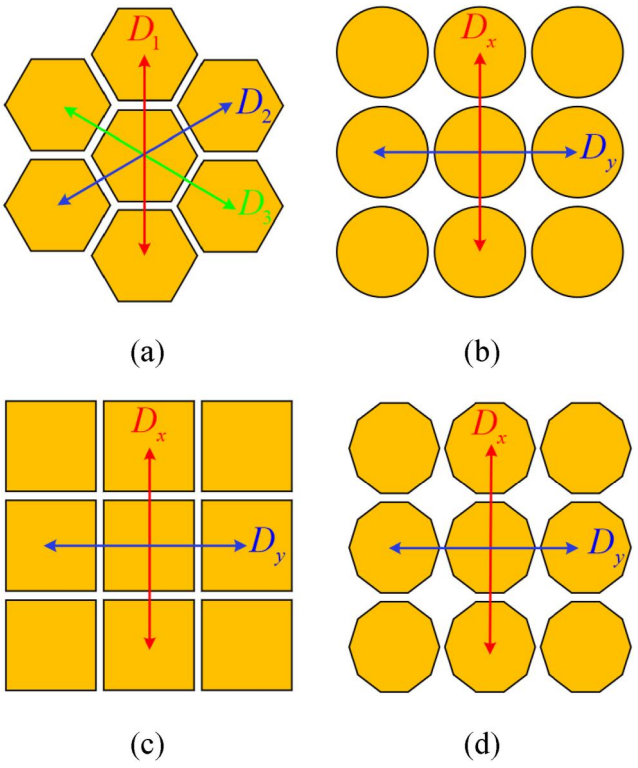

FIGURE 4 Unit cell arrangement. (a) Hexagonal. (b) Circular. (c) Square. (d) Decagon.

In this work, the phase of the unit cell can be modified by adjusting the inner side length (M) of the top regular hexagonal ring and the side length (N) of the bottom regular hexagonal patch. In Figure 5, we study the influence of the unit cell period p and the outer length of the regular hexagonal L on the radiation pattern. As can be seen from Figure 5a, when the unit cell period p increases or decreases, the antenna radiation performance deteriorates and has a higher sidelobe level. As can be seen from Figure 5b, the outer L of the regular hexagon does not affect the elevation performance, and the sidelobe can be maintained at a low level when $L = 8.2$ mm. As a result, the unit cell has a period of $p = 20$ mm, and the outer length of the regular hexagonal is fixed at $L = 8.2$ mm. Hexagonal periodic boundary conditions, along with Floquet port excitations, are established for the unit cell in the CST Microwave Studio for full-wave simulations.

2.3 | PGM structure design

Figure 6 illustrates a circular PGM with a honeycomb lattice, constructed using the optimal set of nine unit cells as described in Section 2.2. The figure indicates that the unit cells arranged in the D_1 direction maintain a consistent size, while those arranged along the D_2 and D_3 directions demonstrate a progressive increase in size. As a result, phase gradients can be observed along the D_2 and D_3 directions, respectively. As shown in Figure 7, the combination of these two vectors, denoted as D_x, represents the overall phase gradient of the PGM along the x-axis.

Table 1 lists the dimensions of nine unit cells and their respective reflection/transmission at an operating frequency of 5.65 GHz. The phase shift resulting from the wave path of the EW radiation generated by the feed and propagating towards

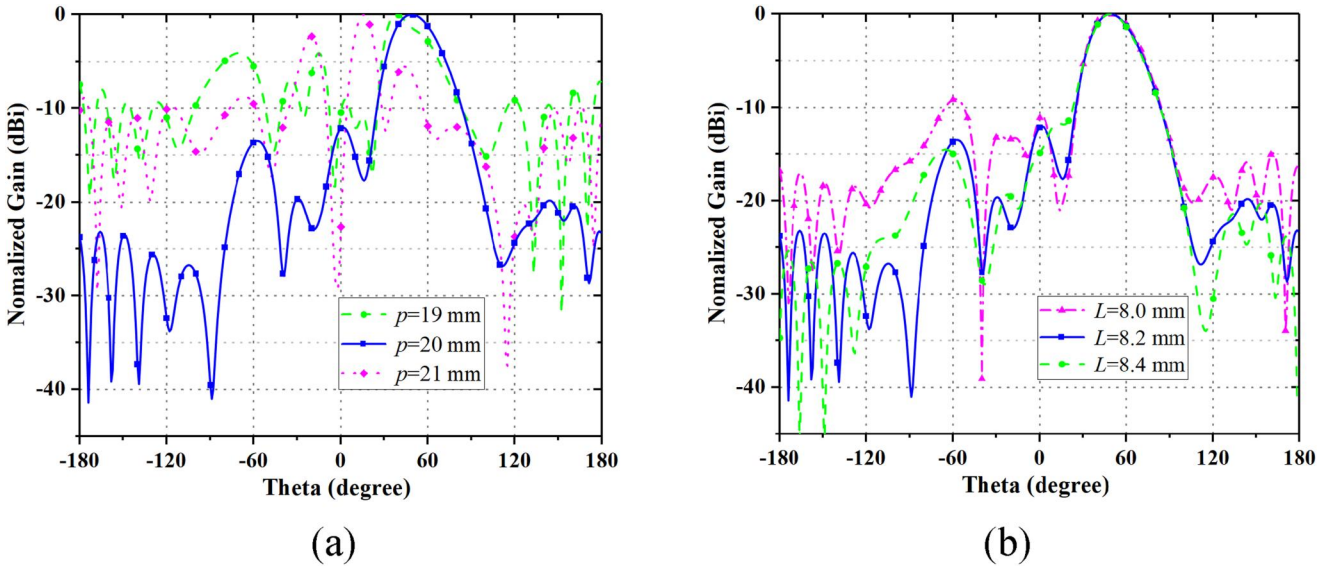

FIGURE 5 The influence of the unit cell period p and the outer length of the regular hexagonal L on the radiation pattern is in State 1. (a) Period p. (b) The outer length of the regular hexagonal L.

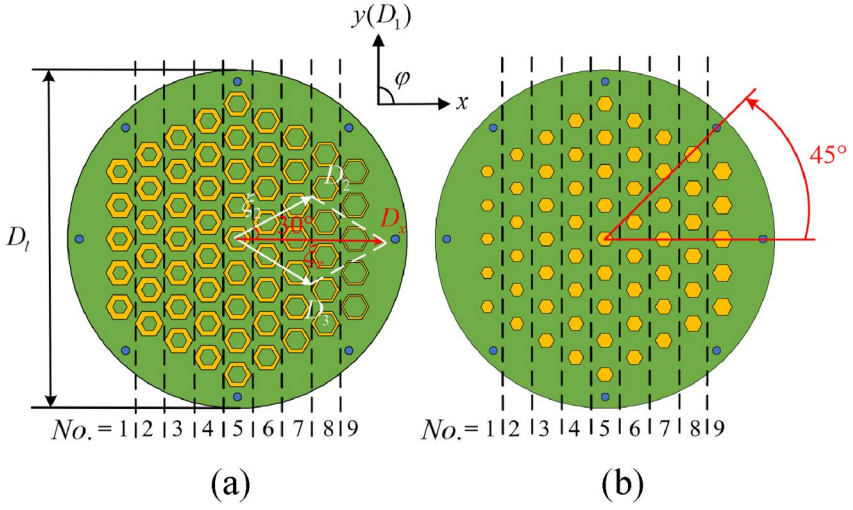

FIGURE 6 Structure of the proposed phase gradient metasurface. (a) Top view. (b) Bottom view.

the individual unit cells of the PRS can be calculated using Equation (4) and subsequently recorded in column 6 of Table 1. Consequently, the combined phase of each unit cell, obtained by superimposing three individual phases, can be determined and recorded in Table 1.

According to Table 1, the phase gradient along D_2 can be calculated as follows:

$$\xi_2 = \frac{\Delta\varphi}{9p} = \frac{\pi(922.2\,^\circ - 264.7^\circ)/180^\circ}{9 \times 20 \times 10^{-3}\ \mathrm{m}} = 62.8\ \mathrm{rad/m} \quad (5)$$

Thus, the phase gradient in the D_x direction can be calculated as follows:

$$\xi_x = 2\xi_2 \cos 30^\circ = 108.7\ \mathrm{rad/m} \quad (6)$$

It is noteworthy that this derived value is close to the theoretically determined phase gradient presented in Section 2.1.

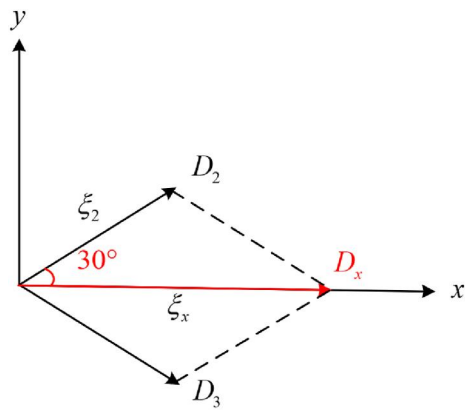

FIGURE 7 Phase gradient analysis of the proposed phase gradient metasurface.

2.4 | Steerable FPRA design

A circular patch antenna is adopted as the feeder, due to its circular symmetry and stable radiation pattern. The circular patch, with a radius of 6.5 mm, is printed on a 1.6-mm-thick FR4 substrate and fed directly through a coaxial probe. According to the ray theory proposed in ref. [29], the FPRA achieves maximum beam gain in the broadside direction when the following resonance condition is satisfied:

$$H = \frac{\lambda_0}{4\pi}\left(\varphi_{\mathrm{PRS}} + \varphi_{\mathrm{ground}}\right) + \frac{\lambda_0}{2}N, N = 0, 1, 2\ldots \quad (7)$$

where φ_{PRS} and $\varphi_{\mathrm{ground}}$ represent the reflection phases of the PRS and ground plane, respectively, while H denotes the cavity height. In this case, we select the reflection phases $\varphi_{\mathrm{PRS}} = 124.6^\circ$ for the unit (i.e. No. = 5) positioned directly above the driven patch. Consequently, the cavity height H is approximately 22 mm. D_l is optimised to 200 mm.

3 | SIMULATION AND MEASUREMENT RESULTS

The performance of the proposed FPRA is simulated using the commercial CST Microwave Studio software. Figure 8a depicts representative 3D radiation beams of the proposed FPRA at 5.65 GHz. The simulation results demonstrate that the main beam continuously steers at 45° intervals in the azimuth plane, while the tilted angle remains fixed around 54° in the elevation plane. The normalised radiation patterns for State 1 at three frequencies are shown in Figure 8b, it can be observed that the main beam remains directionally consistent at 5.55, 5.65 and 5.75 GHz. The integrity of the radiation pattern in all steering directions is maintained over the 5.55–5.75 GHz band, and beam steering covers a fractional bandwidth of 9%. Thereby validating the feasibility of our design. The FPRA achieves a maximum gain of 14.9 dBi, with an aperture efficiency of up to 34.5%. States 3 and 7 exhibit the highest sidelobe levels of −8.0 dB, while the sidelobe levels of

TABLE 1 Dimensions and phase of nine unit cells.

No.	*M* (mm)	*N* (mm)	Reflection phase	Transmission phase	The wave path difference	Phase superposition
1	4.2	3.8	173.2°	−81.4°	830.4°	922.2°
2	4.5	4.2	165.7°	−86.2°	516.9°	596.4°
3	4.8	4.6	152.6°	−94.5°	216.5°	274.6°
4	5.1	4.7	140.2°	−103.1°	163.9°	201°
5	5.4	4.8	124.6°	−114.2°	149.2°	159.6°
6	5.7	4.9	105.8°	−127.6°	163.9°	142.1°
7	6.1	5.0	68.3°	−152.1°	182.1°	98.3°
8	6.5	5.2	15.5°	−178.6°	398.2°	235.1°
9	7.0	5.8	−83.3°	−213.5°	516.5°	264.7°

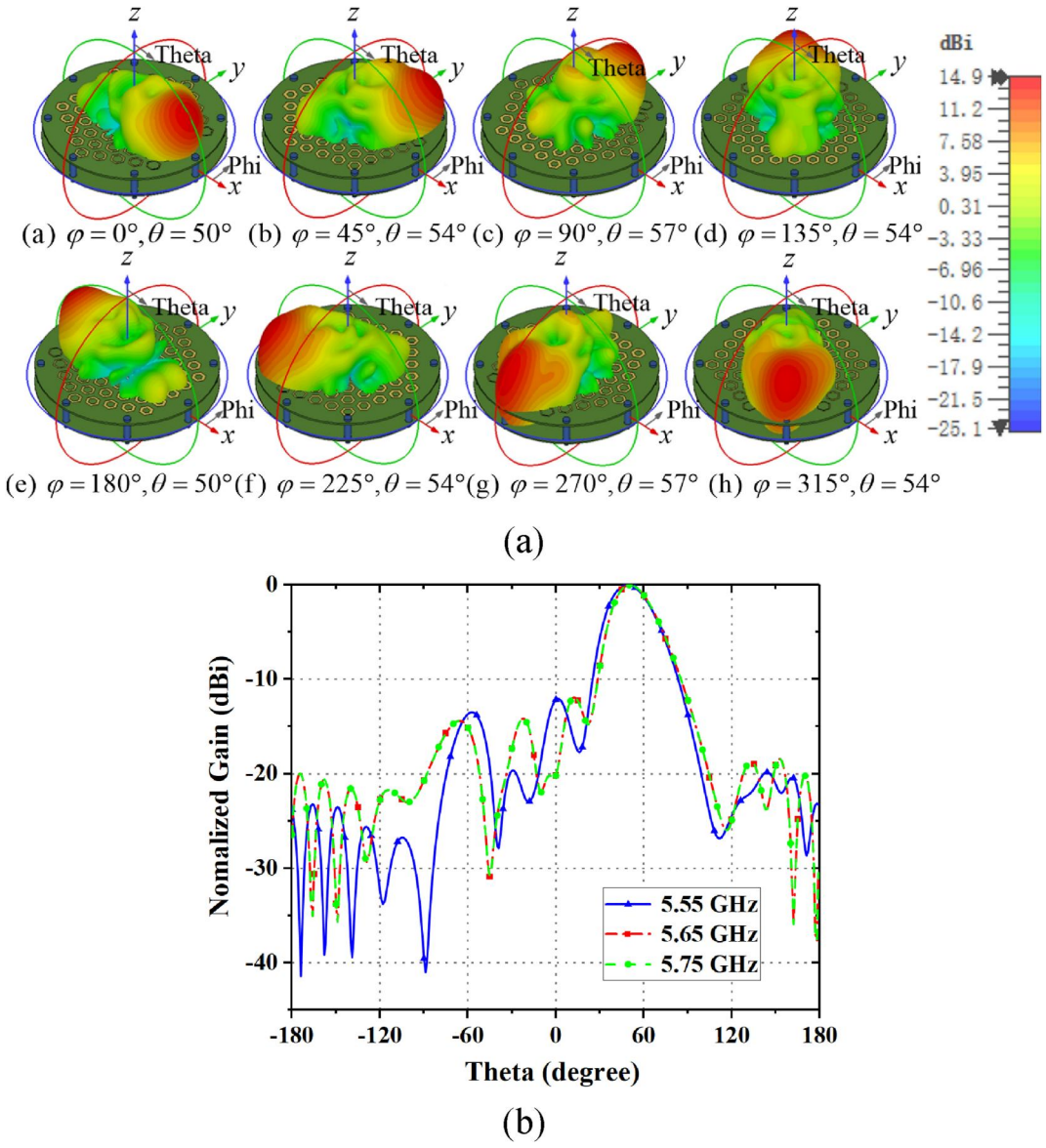

FIGURE 8 Simulated radiation patterns of the proposed FPRA. (a) Simulated 3D radiation patterns of the proposed FPRA at 5.65 GHz. (a) State 1. (b) State 2. (c) State 3. (d) State 4. (e) State 5. (f) State 6. (g) State 7. (h) State 8. (b) State 1: Simulated normalised radiation patterns of the proposed FPRA at 5.55, 5.65 and 5.75 GHz. FPRA, Fabry–Perot resonator antenna.

the remaining states are all below −10 dB. The high sidelobe level at a large deflection angle could be attributed to the edge field of the top PGM. For FPRA, the EW radiated by the feed primarily illuminates the central region of the PGM, resulting in degraded performance of the unit cell positioned at the PGM's edge. At a beam deflection angle as high as 57°, the electric field phase of the edge unit cell deteriorates, leading to degraded sidelobe levels.

Figure 9 plots the measured and simulated reflection coefficients for the eight states. The measured results indicate that all states exhibit an overlapped −10 dB impedance bandwidth ranging from 5.50 to 5.82 GHz, which is consistent with the simulated results. The radiation patterns of the antenna are measured in the anechoic chamber as shown in Figure 10. Eight nylon screws are utilised to ensure the precise assembly of the FPRA between the PGM and the ground plane. Figure 11 shows the radiation patterns in eight states at 5.65 GHz. The beam of

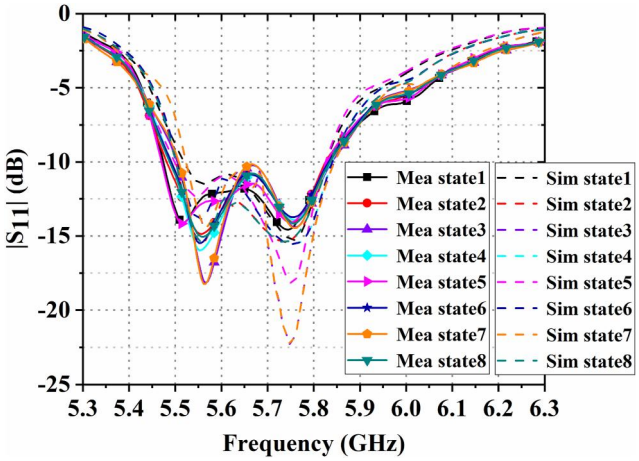

FIGURE 9 Measured and simulated reflection coefficients of the antenna.

FIGURE 10 Fabricated antenna and measurement setup.

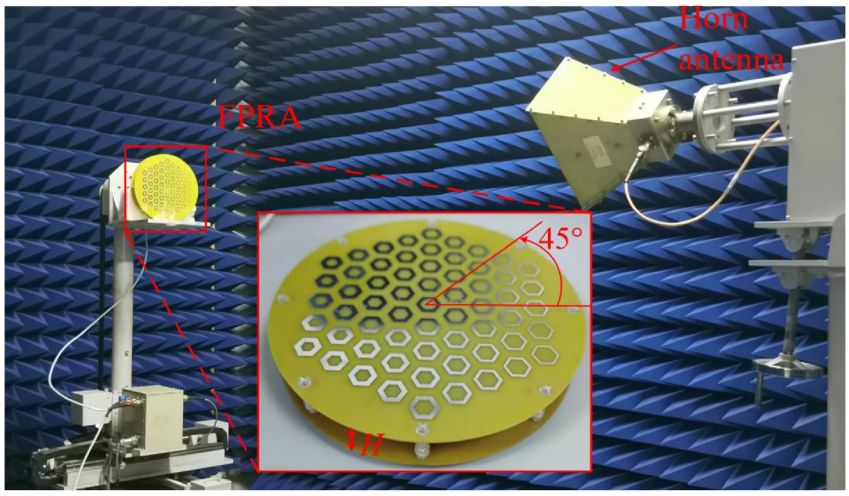

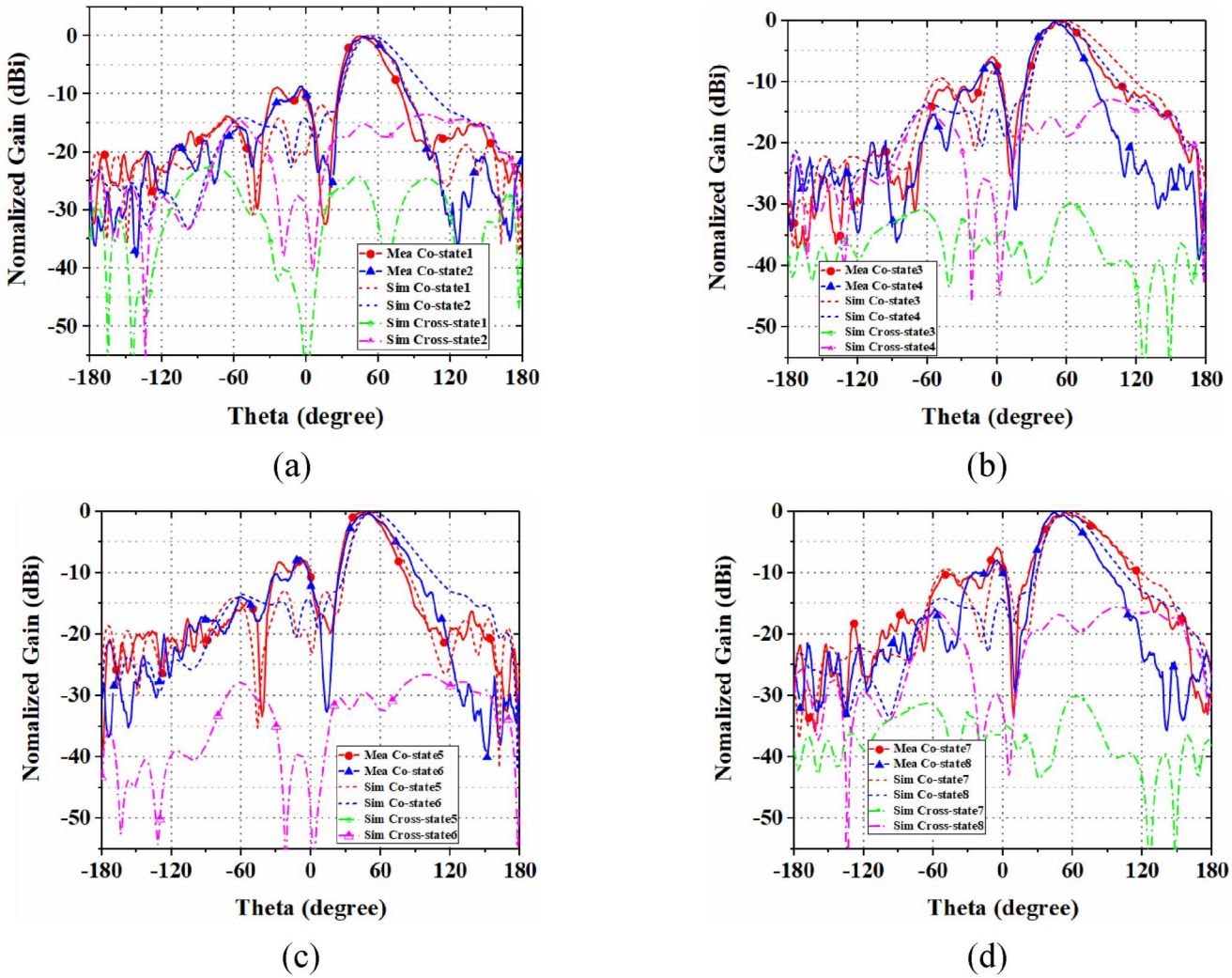

FIGURE 11 Measured and simulated normalised radiation patterns of the proposed Fabry–Perot resonator antenna at 5.65 GHz. (a) States 1 and 2. (b) States 3 and 4. (c) States 5 and 6. (d) States 7 and 8.

the antenna is steered towards the expected direction. The beam elevation remains nearly constant when the PGM is rotated at 45° intervals. However, there is a degree of disagreement between the simulated and measured radiation patterns. The measured results have a much narrower half-power beam width. The main reason is that the mechanical rotation angle is

TABLE 2 Measured and simulated beam directions and their differences.

	Simulation		Measured		Difference	
State	φ	θ	φ	θ	$\Delta\varphi$	$\Delta\theta$
1	0°	50°	0°	45°	0°	5°
2	45°	54°	45°	49°	0°	5°
3	90°	57°	90°	52°	0°	5°
4	135°	54°	135°	49°	0°	5°
5	180°	50°	180°	45°	0°	5°
6	225°	54°	225°	49°	0°	5°
7	270°	57°	270°	55°	0°	2°
8	315°	54°	315°	46°	0°	8°

TABLE 3 Comparison between the proposed antenna and previous designs.

References	Frequency (GHz)	Size	Tilt direction	Tilted angle	Gain (dBi)	Aperture efficiency	Control method
[14]	5.5	$5\lambda \times 0.5\lambda$	1-D	$\pm 25^{\circ}$	13	9.9%	Varactor diodes
[15]	5.5	$5.4\lambda \times 5.4\lambda$	2-D	$\pm 15^{\circ}$	14	10.3%	Varactor diodes
[16]	5.1	$1.6\lambda \times 1.6\lambda$	1-D	$\pm 20^{\circ}$	8.7	24.5%	Liquid metal
[19]	11	$6\lambda \times 6\lambda$	2-D	$\pm 51^{\circ}$	19.4	24.5%	Near-field meta-steering
[21]	21	$92.3\lambda \times 29.4\lambda$	2-D	$\pm 46^{\circ}$	35.75	44.1%	FSS- steering
[31]	5.5	$3.1\lambda \times 3.1\lambda$	1-D	$\pm 15^{\circ}$	16.3	12.7%	PIN diodes
[32]	5.5	$1.8\lambda \times 1.8\lambda$	2-D	$\pm 10^{\circ}$	12.5	21.7%	PIN diodes
This work	5.65	$5.97\lambda \times 1.9\lambda$	1-D	55°	14.9	34.5%	PRS rotation

controlled manually during antenna measurement. In measurement, the tangent plane is not aligned with the tangent plane where the maximum gain point of the radiated beam. Therefore, the measured tangent plane is parallel to the actual tangent plane where the maximum gain is located and there is a distance deviation, resulting in a narrower half-power beam width. The measured results show that in States 1 and 2, the beam directions are tilted towards 45° and 49° in the planes of $\varphi = 0^{\circ}$ and $\varphi = 45^{\circ}$, respectively. The specific beam directions for the other states are provided in Table 2. It summarises the measured and simulated beam directions (φ, θ) along with differences. The measured and simulated azimuths φ are consistent across all states. A slight discrepancy exists between the measured and simulated beam elevation angles, with a maximum error of <8°. This discrepancy can be primarily attributed to measurement errors and inaccuracies in the manufacturing process.

In practical applications, employing a stepper motor offers a promising and convenient approach to enhance the accuracy of beam steering. We will explore and implement this method in our future work.

Table 3 presents a performance comparison between the proposed antenna and other reported antennas in terms of operating frequency, size, and tilt direction. Notably, our proposed method enables continuous 360° beam steering on the azimuth plane and supports significant tilt beams of up to 55° through a simple mechanical rotation mechanism.

4 | CONCLUSION

A novel mechanical beam steering FPRA was designed, fabricated, and measured. The main beam in the azimuth plane is steered by physically rotating the PGM around its central axis. Experimental results demonstrate that the main beam achieves a maximum elevation angle of 55° and a peak gain of 14.9 dBi. The proposed design offers a cost-effective and straightforward solution for beam reconfigurable antennas, eliminating the need for active devices and minimising power consumption.

AUTHOR CONTRIBUTIONS

Yufeng Liu: Supervision; investigation; conceptualization; writing - review & editing. **Lele Zhu**: Software; methodology; validation; data curation; writing - original draft. **Wenmei Zhang**: Funding acquisition; resources; project administration; writing - review & editing. **Wensong Wang**: Writing - review & editing.

ACKNOWLEDGEMENTS

This work was supported by the National Natural Science Foundation of China (Grant 62071282).

CONFLICT OF INTEREST STATEMENT

The authors declare no conflicts of interest.

DATA AVAILABILITY STATEMENT

The data that support the findings of this study are available from the corresponding author upon reasonable request.

ORCID

Yufeng Liu https://orcid.org/0000-0002-5988-0298
Wensong Wang https://orcid.org/0000-0002-5773-8335

REFERENCES

1. Chen, D., et al.: Polarization-reconfigurable and frequency-tunable dipole antenna using active AMC structures. IEEE Access 7, 77792–77803 (2019). https://doi.org/10.1109/access.2019.2919518
2. Luo, Z., et al.: A high-performance nonlinear metasurface for spatial-wave absorption. Adv. Funct. Mater. 32(16), 2109544 (2022). https://doi.org/10.1002/adfm.202109544
3. Ren, J., et al.: Radiation pattern and polarization reconfigurable antenna using dielectric liquid. IEEE Trans. Antenn. Propag. 68(12), 8174–8179 (2020). https://doi.org/10.1109/tap.2020.2996811
4. Schaubert, D.H., et al.: Frequency-agile, polarization diverse microstrip antennas and frequency scanned arrays. U.S. Patent (1983)
5. Wang, Z., et al.: Hybrid metasurface, dielectric resonator, low-cost, wide-angle beam-scanning antenna for 5G base station application. IEEE Trans. Antenn. Propag. 70(9), 7646–7658 (2022). https://doi.org/10.1109/tap.2022.3169067
6. Zhang, X.G., et al.: Pattern-reconfigurable planar array antenna characterized by digital coding method. IEEE Trans. Antenn. Propag. 68(2), 1170–1175 (2019). https://doi.org/10.1109/tap.2019.2938678
7. Xu, R., Chen, Z.N.: A hemispherical wide-angle beamsteering near-surface focal-plane metamaterial Luneburg lens antenna using transformation-optics. IEEE Trans. Antenn. Propag. 70(6), 4224–4233 (2022). https://doi.org/10.1109/tap.2021.3138554
8. Zhang, Z., et al.: A low-profile, Risley-prism-based, beam-steerable antenna employing a single flat prism. IEEE Trans. Antenn. Propag. 70(8), 6646–6658 (2022). https://doi.org/10.1109/tap.2022.3161562
9. Wang, Y., Zhang, A.: Dual circularly polarized Fabry-Perot resonator antenna employing a polarization conversion metasurface. IEEE Access 9, 44881–44887 (2021). https://doi.org/10.1109/access.2021.3062460
10. Zhou, L., et al.: High directivity Fabry-Perot antenna with a nonuniform partially reflective surface and a phase correcting structure. IEEE Trans. Antenn. Propag. 68(11), 7601–7606 (2020). https://doi.org/10.1109/tap.2020.2982514
11. Guan, Y., et al.: Wideband and compact Fabry-Perot resonator antenna using partially reflective surfaces with regular hexagonal unit. IEEE Antenn. Wireless Propag. Lett. 20(6), 1048–1052 (2021). https://doi.org/10.1109/lawp.2021.3070376
12. Ji, L.Y., et al.: One-dimensional beam-steering Fabry-Perot cavity (FPC) antenna with a reconfigurable superstrate. Int. J. Microw. Wirel. Technol. 12(3), 1–7 (2019). https://doi.org/10.1017/s1759078719001144
13. Ji, L.Y., Zhang, Z.Y., Liu, N.W.: A two-dimensional beam-steering partially reflective surface (PRS) antenna using a reconfigurable FSS structure. IEEE Antenn. Wireless Propag. Lett. 18(6), 1076–1080 (2019). https://doi.org/10.1109/lawp.2019.2907641
14. Guzman-Quiros, R., et al.: Electronic full-space scanning with 1-D Fabry-Pérot LWA using electromagnetic band-gap. IEEE Antenn. Wireless Propag. Lett. 11, 1426–1429 (2012). https://doi.org/10.1109/lawp.2012.2228624
15. Guzmán-Quirós, R., et al.: A Fabry-Pérot antenna with two-dimensional electronic beam scanning. IEEE Trans. Antenn. Propag. 64(4), 1536–1541 (2016). https://doi.org/10.1109/tap.2016.2525832
16. Yang, X., et al.: A radiation pattern reconfigurable Fabry-Pérot antenna based on liquid metal. IEEE Trans. Antenn. Propag. 68(11), 7658–7663 (2020). https://doi.org/10.1109/tap.2020.2993310
17. Katare, K.K., et al.: Beam-switching of Fabry-Perot cavity antenna using asymmetric reflection phase response of bianisotropic metasurface. IET Microw. Antenn. Propag. 13(6), 842–848 (2019). https://doi.org/10.1049/iet-map.2018.5529
18. Wan, X., et al.: Horn antenna with reconfigurable beam-refraction and polarization based on anisotropic Huygens metasurface. IEEE Trans. Antenn. Propag. 65(9), 4427–4434 (2017). https://doi.org/10.1109/tap.2017.2722829
19. Afzal, M.U., Esselle, K.P.: Steering the beam of medium-to-high gain antennas using near-field phase transformation. IEEE Trans. Antenn. Propag. 65(4), 1680–1690 (2017). https://doi.org/10.1109/tap.2017.2670612
20. Ahmed, F., Singh, K., Esselle, K.P.: State-of-the-art passive beam-steering antenna technologies: challenges and capabilities. IEEE Access 11, 69101–69116 (2023). https://doi.org/10.1109/access.2023.3278570
21. Wen, Z.-Y., et al.: A dual-layer full-phase frequency-selective surface for continuous 2-D beam scanning. IEEE Trans. Antenn. Propag. 70(11), 10706–10717 (2022). https://doi.org/10.1109/tap.2022.3209224
22. Yu, N., et al.: Light propagation with phase discontinuities: generalized laws of reflection and refraction. Science 334(6054), 333–337 (2011). https://doi.org/10.1126/science.1210713
23. Luo, Z., et al.: Anisotropic and nonlinear metasurface for multiple functions. Sci. China Inf. Sci. 64(9), 1–10 (2021). https://doi.org/10.1007/s11432-021-3264-9
24. Chen, J., et al.: Wideband leaky-wave antennas loaded with gradient metasurface for fixed-beam radiations with customized tilting angles. IEEE Trans. Antenn. Propag. 68(1), 161–170 (2019). https://doi.org/10.1109/tap.2019.2940542
25. Cui, T.J., et al.: Coding metamaterials, digital metamaterials and programmable metamaterials. Light Sci. Appl. 3(10), e218 (2014). https://doi.org/10.1038/lsa.2014.99
26. Singh, K., et al.: Controlling the most significant grating lobes in two-dimensional beam-steering systems with phase-gradient metasurfaces. IEEE Trans. Antenn. Propag. 68(3), 1389–1401 (2019). https://doi.org/10.1109/tap.2019.2955244
27. Zhang, W., et al.: Wideband RCS reduction of a slot array antenna using phase gradient metasurface. IEEE Antenn. Wireless Propag. Lett. 17(12), 2193–2197 (2018). https://doi.org/10.1109/lawp.2018.2870863
28. Kiris, O., Topalli, K., Unlu, M.: A reflectarray antenna using hexagonal lattice with enhanced beam steering capability. IEEE Access 7, 45526–45532 (2019). https://doi.org/10.1109/access.2019.2909313
29. Trentini, G.V.: Partially reflecting sheet arrays. IRE Trans. Antenn. Propag. AP-4(4), 666–671 (1956). https://doi.org/10.1109/tap.1956.1144455
30. Ratni, B., et al.: Design of phase-modulated metasurfaces for beam steering in Fabry-Perot cavity antennas. IEEE Antenn. Wireless Propag. Lett. 16, 1401–1404 (2017). https://doi.org/10.1109/lawp.2016.2639463
31. Ji, L.-Y., et al.: A reconfigurable partially reflective surface (PRS) antenna for beam steering. IEEE Trans. Antenn. Propag. 63(6), 2387–2395 (2015). https://doi.org/10.1109/tap.2015.2412143
32. Xie, P., et al.: A dual-polarized two-dimensional beam-steering Fabry-Pérot cavity antenna with a reconfigurable partially reflecting surface. IEEE Antenn. Wireless Propag. Lett. 16, 2370–2374 (2017). https://doi.org/10.1109/lawp.2017.2718567

How to cite this article: Liu, Y., et al.: Mechanical azimuthal beam-steering Fabry–Perot resonator antenna with large deflection angle. IET Microw. Antennas Propag. 18(6), 413–421 (2024). https://doi.org/10.1049/mia2.12471